Nonequilibrium phase transitions of a nematic liquid crystal under ac field-driven electroconvection

Jong-Hoon Huh

Department of Physics and Information Technology, Faculty of Computer Science and Systems Engineering, Kyushu Institute of Technology, Fukuoka 820-8502, Japan

(Received 17 November 2021; accepted 16 June 2022; published 1 July 2022)

We report on phase transitions between isotropic and nematic liquid crystal phases in nonequilibrium systems (NESs). ac field-driven electroconvection (EC) provides an NES, which can be well controlled by the voltage V and frequency f; it arises electrohydrodynamically at a threshold voltage V_c. In continuous cooling and heating processes with various rates R, the critical temperature T_c was determined at a critical time t_c for phase transitions. Moreover, the morphological and dynamical features in the phase transitions were examined using an electro-optical image processing method. In comparison with an equilibrium system ($V = 0$), two typical turbulent ECs (i.e., NESs), which are called dynamic scattering mode 1 (DSM1 for $V > V_c$) and DSM2 (for $V \gg V_c$), were examined to understand the nonequilibrium phase transitions. In particular, our results show that in high voltage-induced turbulence (i.e., DSM2), T_c can be determined effectively without considering R; this provides a possibility for a material technology application in nonequilibrium-based circumstances.

DOI: 10.1103/PhysRevE.106.014702

I. INTRODUCTION

Phase transitions are among the most important subjects of material science [1]; their features are the main issues of fundamental physics [2–4] and play a crucial role in a variety of application fields from natural materials [5,6] to artificial matters [7,8]. Moreover, bifurcations are widely addressed as a transition between two states that are qualitatively distinguished from each other; in particular, they are found in research fields for nonequilibrium systems (NESs) and nonlinear dynamics [9,10]. The present electroconvection (EC) of nematic liquid crystals (NLCs) is an attractive system for revealing phase transitions in nonequilibrium states provided by various pattern bifurcations [11–13]. Note that in the EC system dissipative structures occur and evolve into more complicated ones as bifurcation phenomena [14,15]; generally, in equilibrium systems (ESs) such dissipative macroscopic structures are not found [14,15].

The well-known fundamental phase transition from the isotropic phase (ISO) to the NLC phase in ESs has been successfully understood [16–18]; the phases indicating the order of rodlike molecules are strictly defined by the order parameter S. In conventional analysis, the phase transition is determined by $S = \frac{1}{2}\langle 3\cos^2\theta - 1\rangle$, which is defined by an angle θ of each molecule with respect to the director; for example, $S = 0$ for ISO, $0 < S < 1$ for NLC, and $S = 1$ for crystals [17,18], where the director is defined by a unit vector $\boldsymbol{n}$ ($\equiv -\boldsymbol{n}$) indicating a locally averaged direction of the molecules [17,18]. A quantitative understanding of the phase transition in ESs provides us with useful applications and technologies such as smart liquid crystal displays [19,20] and microactuators [21,22]. In this study, we address phase transitions in NESs caused by EC and consider a possibility of a material technology application in nonequilibrium-based circumstances [23,24]. We need to mention first that our nonequilibrium phase transitions should be distinguished from those under initial temperatures and cooling rates [25]; in this study, ac field-induced EC provides the NES, and the voltage strength varies the degree of the NES. Moreover, our nonequilibrium phase transitions should be distinguished from those in dc or ac fields that do not cause EC [18].

The EC has been extensively investigated to understand the fundamental physics of the NES [11–15], since Williams discovered Williams domains (WDs) [26] and Carr and Helfrich provided a persuasive mechanism [27]; hereafter, the mechanism will be called the Carr-Helfrich mechanism (CHM). According to the CHM [27], a fundamental EC (i.e., WD) [11–13,26] can be induced by a type of coupling between the director field and flows resulting from electric charges under an electric field $E(t) = E_0\cos(2\pi ft)$ across a thin-layer NLC (typically of thickness $d = 10$–$100\,\mu$m) between parallel electrodes. Fluctuations of the initial director $\boldsymbol{n}_0$ triggered by thermal noise can be reinforced by a material flow resulting from the Coulomb force acting on space charges that are locally focused by electric anisotropy of the NLC. Accordingly, if the Coulomb force overcomes the viscoelastic and dielectric restoring force above a threshold voltage V_c, an electrohydrodynamic instability arises in the NLC layer; $V_c = V_c(f)$ is well validated [11–13]; V_c is approximately 7 V (at $f = 100$ Hz) in the present NLC (see below). As a result, EC is induced and optically observed using a polarization microscope [17,18]. If one prepares sample cells with $\boldsymbol{n}_0 = (1, 0, 0)$, which are called planar alignment cells, periodic rolls (i.e., WD) along the y axis are observed through a lens effect resulting from the periodically modulated director field [$\boldsymbol{n} = (n_x, 0, n_z)$]. Thus, the wave vector $\boldsymbol{k}_{\rm WD}$ is parallel to $\boldsymbol{n}_0$ (i.e., $\boldsymbol{k}_{\rm WD} \| \boldsymbol{n}_0$). In contrast, in the case of a so-called homeotropic alignment cell [$\boldsymbol{n}_0 = (0, 0, 1)$] used in this study, the soft-mode turbulence

(SMT) arises at V_c [28,29], showing random wave vectors $\boldsymbol{k}_{SMT}$ because of the continuously rotating mode of the $\boldsymbol{C}$ director resulting from a Fréedericksz transition (FT) at V_F ($< V_c$), where the $\boldsymbol{C}$ director indicates a projected vector of the $\boldsymbol{n}$ director into the xy plane; V_F is independent of f. Typically, V_F is approximately 4 V in the present NLC (see below) [17,18,29,30].

By increasing V, successive pattern evolutions are found [12,13]; in particular, EC-developed turbulences, namely dynamic scattering mode 1 (DSM1) and dynamic scattering mode 2 (DSM2), are found for $V > V_c$ and $V \gg V_c$, respectively [12,19,31]; $e = V/V_c > 2.2$ for DSM1 and $e > 3.3$ for DSM2 in Ref. [31]. Both are clearly distinguished from each other in optical observation and analysis [12,32] (see below). Note that the DSM2 was the basic phenomenon of developed liquid crystal displays [19].

In this study, we examined the phase transitions between the ISO ($S = 0$) and NLC ($S \neq 0$) phases. In this paper, I-N and N-I transitions indicate ISO-NLC and NLC-ISO transitions, respectively. In particular, in comparison with those in ESs ($V = 0$), the phase transitions in NESs (i.e., DSM1 and DSM2) are determined in the continuous cooling transformation (CCT) and continuous heating transformation (CHT) processes [33–35] using dynamic analysis for time-dependent optical images. Generally, isothermal processes such as time-temperature transformation (TTT) are widely used for phase transitions such as crystallization of metals from liquid states [33,36,37]. In this study, we present the findings in CCT and CHT processes and briefly compare them in the TTT processes after cooling and heating treatments.

The remainder of this paper is organized as follows. The details of the sample cell, the experimental apparatus, and the techniques used are described in Sec. II. In Secs. III A and III B, the I-N and N-I transitions in ESs (i.e., $V = 0$) and in NESs (i.e., $V > V_c$) are presented, and the experimental findings in ESs and NESs are compared; and a theoretical result for ESs ($V \neq 0$ but no EC) is discussed to determine if it can be expanded to the present NES accompanying EC (i.e., DSM1 and DSM2). In Sec. III C, the morphological and dynamical features of the phase transitions in NESs are described. In Sec. IV, our findings on the phase transitions in NESs are summarized, and the prospects for future study are discussed.

II. EXPERIMENT

To investigate the phase transitions between the ISO and NLC phases, a typical, thermotropic NLC [*p*-methoxybenzylidene-*p*′-*n*-butylaniline (MBBA)] was used; its important parameters for EC, electric conductivity $\sigma_{||} = 6.3 \times 10^{-7}\,\Omega^{-1}\,m^{-1}$ and dielectric constant $\varepsilon_{||} = 4.5$, were measured at a temperature $T = 25\,^{\circ}C$ using an LCZ meter ($f = 100$ Hz). Here, the subscript $\|$ indicates the orientation parallel to the initial director $\boldsymbol{n}_0$ in a homeotropically aligned sample cell [$\boldsymbol{n}_0 = (0, 0, 1)$] as shown in Fig. 1. To induce EC (i.e., NES), a voltage $V(t) = E(t)d = \sqrt{2}V\cos(2\pi ft)$ was applied across a slab of the NLC ($d = 50\,\mu m$) sandwiched between two parallel transparent electrodes (indium tin oxide) where $f = 100$ Hz was fixed. Moreover, a temperature controller (TH-99, Japan Hightech) was used to perform the phase transitions [refer to $T(t)$ in Fig. 1]. The error of measurements of T was below $\pm 0.2\,^{\circ}C$ in this study. To show $T(t)$ at different cooling and heating rates R, some typical curves of $T(t)$ are plotted in Fig. 2,

$$T(t) = T_0^{\pm} \pm Rt, \tag{1}$$

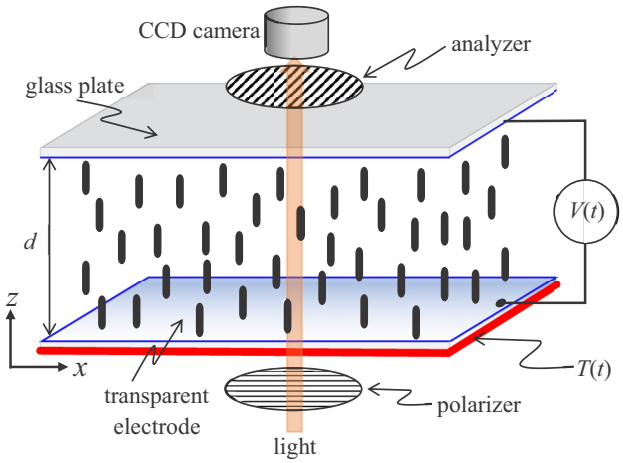

FIG. 1. Experimental setup and a homeotropically aligned cell [$\boldsymbol{n}_0 = (0, 0, 1)$]. $V(t)$ and $T(t)$ denote a voltage generator and a temperature controller, respectively. As required, a polarizer and an analyzer are inserted or removed; the charge-coupled device (CCD) camera records optical images in the xy plane. The black rods indicate the director $\boldsymbol{n}$ of a nematic liquid crystal (NLC). There may be a time lag between the sample and the hot stage that is caused in the measurement of temperature of the NLC. Fortunately, such a time lag causing a temperature lag was less than a few seconds, and was neglected in comparison with the data of T_c at t_c (about 10^2–10^3 s) in Figs. 3–6.

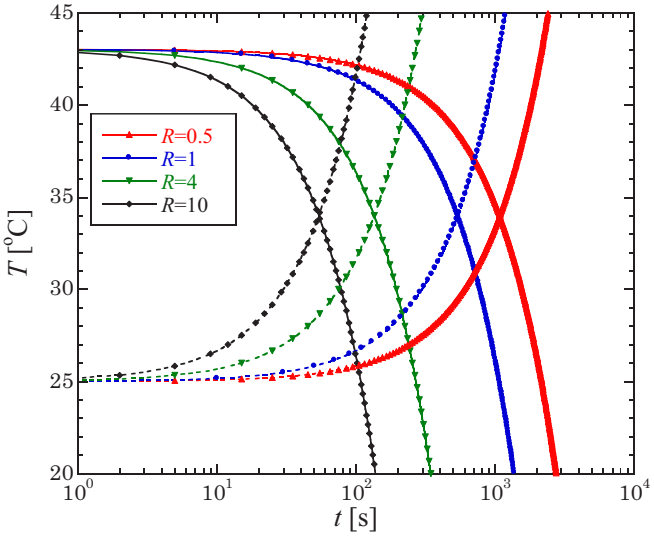

FIG. 2. Temperature T as a function of time t with respect to various cooling and heating rates $R = 0.1$–$10\,(^{\circ}C/min)$: in this study, $T = T_0^- - Rt$ for the cooling process and $T = T_0^+ + Rt$ for the heating process. T_0^- (= 43 °C) and T_0^+ (= 25 °C) indicate starting temperatures for the cooling and heating processes, respectively.

where ± corresponds to heating (+) and cooling (−) processes, respectively, and $T_0^{\pm}$ denotes the starting temperature (e.g., $T_0^{+} = 25\,^{\circ}$C for heating and $T_0^{-} = 43\,^{\circ}$C for cooling in Fig. 2).

The standard shadowgraph method was used for optical observations and measurements [17,18]; if needed, a polarizer (P) and an analyzer (A) could be inserted or removed [38,39]. The EC patterns and their dynamics were observed using computer-controlled image software (SCION IMAGE) and an image-capture board (Scion Corp., PCI-VE5) together with a charge-coupled device (CCD) camera (Sony, XC-75) mounted on a polarizing microscope (Olympus, ML9300) and all optical patterns were observed in the xy plane [30,39].

III. RESULTS AND DISCUSSION

A. I-N and N-I transitions in an equilibrium system

First, we examined the phase transitions in ES ($V = 0$). For $R = 10\,^{\circ}$C/min in the cooling and heating processes, transmitted optical intensities $I(t)$ are displayed in Fig. 3(a); $I(t_n)$ at $t = t_n$ (with $\Delta t = t_{n+1} - t_n = 1$ s) was averaged in each image with 256×256 pixels ($\approx 420 \times 420\ \mu$m) [e.g., Fig. 3(b)]; $I(t_n) = \frac{1}{(256)^2}\sum_{x,y=0}^{255} I(x, y)$ for $0 \leqslant n \leqslant 3600$. Hereafter, the units of $R(^{\circ}\text{C/min})$, $T\,(^{\circ}\text{C})$, and t (s) including their characteristic values (e.g., R_c, T_c^*, and t_{R0}) are omitted for convenience. The profiles of $I(t)$ and $T(t)$ for the cooling and heating processes determine the critical temperature T_c and time t_c for the I-N and N-I transitions. In this study, t_c is defined by a minimal peak, as shown in Fig. 3(a). Then, T_c is calculated using Eq. (1). For example, because $t_c(\text{I-N}) = 79$ in $I(t)$ for the cooling process, $T_c(\text{I-N}) = 29.83$ is determined by Eq. (1). Moreover, to observe the I-N transition, some optical patterns providing $I(t)$ are displayed in Fig. 3(b). The patterns at $t = 70$ and 110 correspond to the ISO and NLC phases, respectively, and the latter can be differentiated from the former by disclinations of the NLC found in the present homeotropically aligned cell; refer to the complicated curves implying disclinations in the NLC ($t = 110$). Note typical patterns for initiating the I-N transition ($t_c = 79$) and for the growth of localized NLC states (in closed curves) in the ISO phase ($t_c = 94$).

By measuring T_c in various R (= 0.1–10) in the same way [Fig. 3(a)], a CCT diagram is plotted in Fig. 4, and $T(t)$ for three values of R [i.e., Eq. (1)] was used to easily understand $T_c(t)$. Considering an estimated CCT curve [$T_c(t)$] between the NLC and crystal (CRYST) phases, the three typical phases can be characterized in such a dynamic process; in fact, more complicated transitions including a glass transition depending on R may be described [25]. From this diagram, an extremely slow cooling method (i.e., $R \to 0$) can determine the nominal value of the phase-transition temperature for the I-N transition (i.e., T_{IN}) to which $T_c(t)$ approximates for $t \to \infty$; this value is quite consistent with that reported in different measurements such as nuclear magnetic resonance (NMR) [40], but it is slightly lower than that in measurements of relaxation time and refractive index [41]. Furthermore, it can be estimated that an extremely fast cooling method (i.e., $R > R_c$) cannot cause the I-N phase transition; that is, the ISO phase can be sustained, even though it may be unstable (see below).

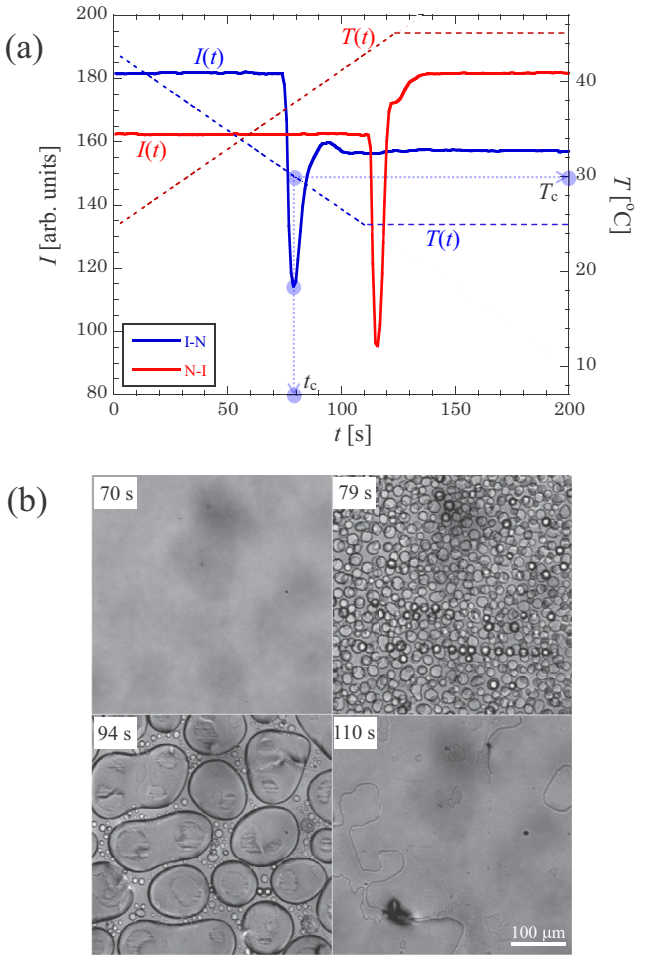

FIG. 3. Phase transitions between isotropic (ISO) and NLC phases in the equilibrium system (ES, i.e., $V = 0$). (a) Averaged optical intensity I as functions of t in the cooling and heating processes at a fixed $R = 10\,(^{\circ}\text{C/min})$, and (b) corresponding patterns at times for the isotropic-nematic (I-N) transition. A critical time t_c is measured at the minimal peak of $I(t)$, and then a critical temperature T_c is calculated at $t = t_c$ by Eq. (1). For example, $T_c = 29.83\,^{\circ}$C at $t_c = 79$ s; T_c and t_c are also determined in the nematic-isotropic (N-I) transition in the same way.

Intuitively, a minimal finite time ($t_c \neq 0$) for ordering ($S \neq 0$) of molecules is needed for the I-N transition; that is, it takes time to form a critical size of nucleation for the NLC [33]. Therefore, the I-N transition may occur for $R < R_c$ (see below).

The curve of $T_c(t)$ can be expressed by an appropriate function:

$$T_c(t) = T_{c0} + \delta_c \text{arcsec}[b_c \log_{10}(10 + t - t_c^*)]. \qquad (2)$$

The curve shows a universal shape for various materials [33–35]; $T_{c0} = 24.65$, $\delta_c = 10.79$, $b_c = 0.8660$, and $t_c^* = 75.20$ in this study; accordingly, a characteristic temperature $T_c^* = 24.65$ at $t = t_c^*$ is found. Thus, the estimated curve of $T(t)$ for the critical rate R_c should be crossed over the curve of $T_c(t)$ at the characteristic time t_c^* [33], which means that the I-N transition can be observed for $R < R_c$. In this study, R_c (= 14.64) can be calculated by inserting T_c^* and t_c^* into

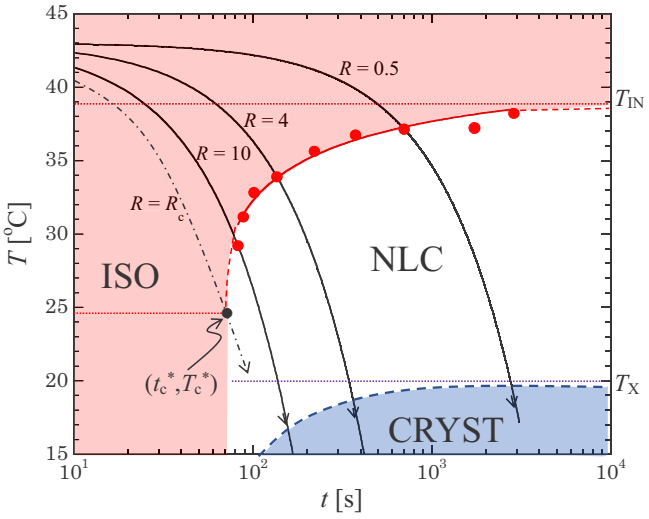

FIG. 4. Continuous cooling transformation (CCT) diagram. The CCT curve was measured by various cooling rates $R = 0.1$–10 (°C/min), and the corresponding curve (thick red line) was fitted by Eq. (2). ISO, NLC, and CRYST indicate isotropic, nematic liquid crystal, and crystal phases, respectively. T_{IN} and T_X denote characteristic temperatures for the I-N transition and for the NLC-CRYST transition, respectively (for $t = 10^4$ s). The broken lines including a CCT curve for the NLC-CRYST transition are estimated, and the broken dotted line indicates a $T(t)$ curve for a critical R_c that is a maximal value for measuring the I-N transition.

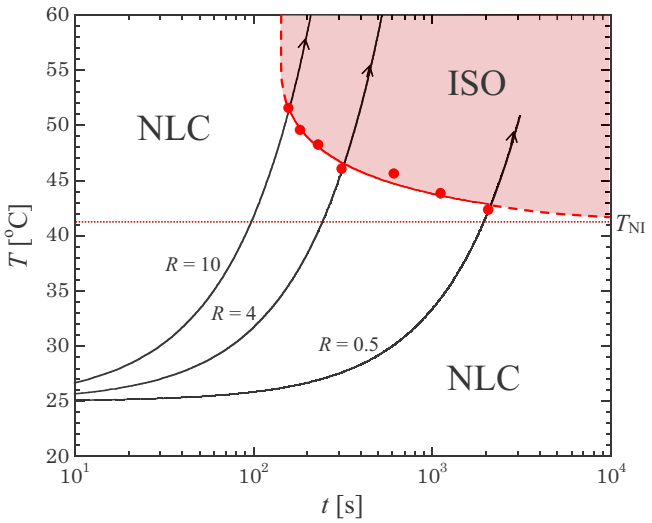

FIG. 5. Continuous heating transformation (CHT) diagram. The CHT curve (thick red line) was measured by various heating rates $R = 0.1$–10(°C/min) and was fitted by Eq. (3). T_{NI} denotes a characteristic temperature for the N-I transition (for $t = 10^4$ s), i.e., the so-called melting point (T_m). The broken lines are estimated.

Eq. (1), which is larger than the maximum value of our temperature controller, $R = 10$. Considering the practical time of actual experiments (e.g., $t < 10^4$ in this study), $T_c \to T_{IN} = 38.44$ in Eq. (2) is well satisfied with the value estimated in Fig. 4 ($t = 10^4$) [40].

In contrast, in the same way, a CHT diagram is plotted in Fig. 5; $T_c(t)$ divides ISO from NLC through continuous heating processes with various R ($= 0.1$–10). Similar to the CCT diagram (Fig. 4), the phase-transition temperature T_{NI} for the N-I transition is also estimated by considering a sufficiently slow heating (i.e., $R \to 0$). Moreover, an extremely fast heating method (i.e., $R > R_c$) cannot cause the phase transition so that the NLC phase may be sustained as an unstable state; similar to the CCT diagram (Fig. 4), a minimal finite time ($t_c \neq 0$) for disordering ($S = 0$) of the molecules may be needed for the N-I transition. Furthermore, the CHT curve [$T_c(t)$] can be expressed by using Eq. (3):

$$T_c(t) = T_{h0} + \delta_h \mathrm{arccsc}[b_h \log_{10}(10 + t - t_c^{**})]. \qquad (3)$$

In this study, $T_{h0} = 34.70$, $\delta_h = 19.60$, $b_h = 0.7658$, and $t_c^{**} = 112.4$. In the same way explained for the CCT diagram, T_c^{**} ($t = t_c^{**}$) $= 65.49$ and $R_c = 21.61$ (not seen in Fig. 5). Similar to the I-N transition (Fig. 4), the N-I transition can occur for $R < R_c$ [33]. It is found that $T_c \to T_{NI} = 41.32$ for $t = 10^4$ in this study; that is, the calculated $T_{NI}(t = 10^4)$ by considering the practical time of actual experiments is well satisfied with the value estimated from the experimental result in Fig. 5. Usually, the difference in the phase-transition temperatures, $T_{NI} - T_{IN}$ (~ 2.9 at $t = 10^4$), has been known in various measurements such as differential scanning calorimetry (DSC) [42], which can result from a hysteric phenomenon on ordering ($S \neq 0$) and disordering ($S = 0$) between the NLC and ISO phases [43]; see also Fig. 3(a). This indicates that the phase transition is subcritical [14] (see below).

B. Comparison between equilibrium and nonequilibrium systems on CCT and CHT diagrams

Next, we examined the phase transitions in NES ($V > V_c$); in the presence of V, T_c was measured by continuous cooling and heating processes [Fig. 3(a)]. DSM1 ($V = 28.4$ V) and DSM2 ($V = 92.1$ V) were used as the NES; they are optically distinguished from each other, as shown in the inserted snapshot in Fig. 6. The snapshot shows a transient state from DSM1 to DSM2 by increasing V. Note that DSM2 characterized by complicated disclinations is distinguishable from DSM1 without them [12,32]. Moreover, DSM2 shows spatial isotropy in optical properties whereas DSM1 has anisotropy [12,32]; as a result, both provide different dynamics [44]. To determine CCT and CHT diagrams (Fig. 6), pure DSM1 and DSM2 (completely developed from DSM1) were used.

In Fig. 6, the CCT and CHT curves of DSM1 and DSM2 are plotted in comparison with those of the ES ($V = 0$). Overall, the curves shifted towards lower temperatures than those of the ES. Therefore, the phase-transition temperatures, T_{IN} and T_{NI} (for $t = 10^4$), in the NES were also lower than those in the ES. In particular, the shift of the CCT curves appears to be more noticeable than that of the CHT curves, as shown in Fig. 6 (also refer to Figs. 7 and 8). This means that the effect of the electric field for ordering to the NLC phase is stronger than that for disordering to the ISO phase. Moreover, the results are plotted as $T_c(R)$ in Fig. 7. The difference in critical temperatures, $\Delta T_c = T_c(\mathrm{CHT}) - T_c(\mathrm{CCT})$, decreases with decreasing R; such behavior is not changed by V. In this experiment, it seems that $\Delta T_c \approx 0$ (i.e., $T_{NI} \approx T_{IN}$) for $R \to 0$, which may not depend on the ES and NES. Evidently, the

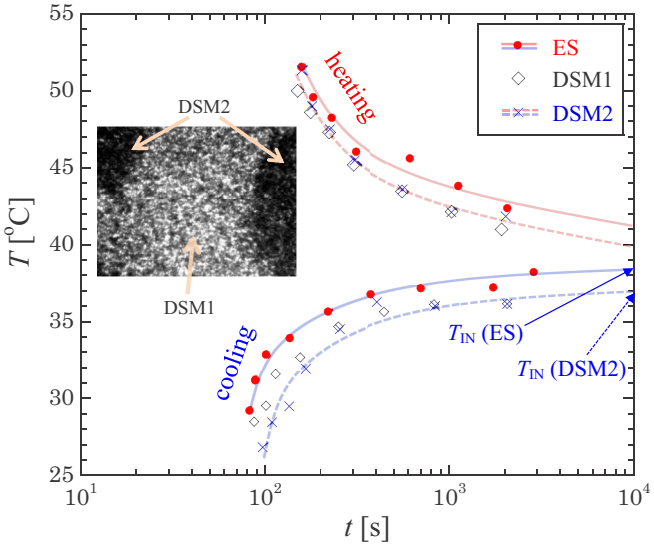

FIG. 6. CCT and CHT diagrams with respect to ES ($V = 0$), DSM1 ($V = 28.4$ V), and DSM2 ($V = 92.1$ V). Both dynamic scattering modes (DSM1 and DSM2) can be distinguished from each other through their optical patterns displayed as an inset. In comparison with those of ES, such CCT and CHT, curves of nonequilibrium systems (NESs, i.e., DSM1 and DSM2) shift to lower temperatures; consequently, T_{IN} (ES) > T_{IN} (DSM2) and T_{NI} (ES) > T_{NI} (DSM2).

ΛT_c dependence on R indicates that the phase transition is subcritical [14].

In Fig. 7, T_c can be expressed by

$$T_c = T_{cR0}^{\pm} \pm a(R/R_c)^{\beta}. \tag{4}$$

Here, $T_{cR0}^{\pm}$ indicates a characteristic value of T_c ($R \to 0$) for heating (+) and cooling (−) processes, and a and β are determined by the least square method; all of them appear

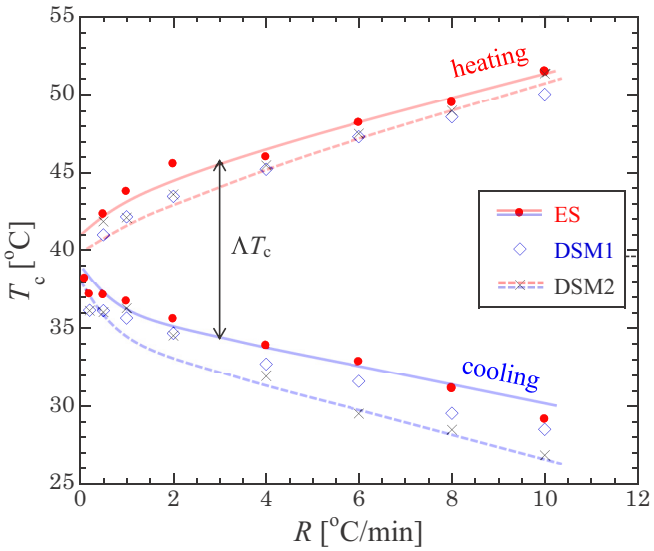

FIG. 7. Critical temperature $T_c(R)$ in the cooling and heating processes. In comparison with those of ESs ($V = 0$), the curves of NESs (i.e., DSM1 and DSM2) shift to lower temperatures. The conditions of DSM1 and DSM2 are the same to those of Fig. 6.

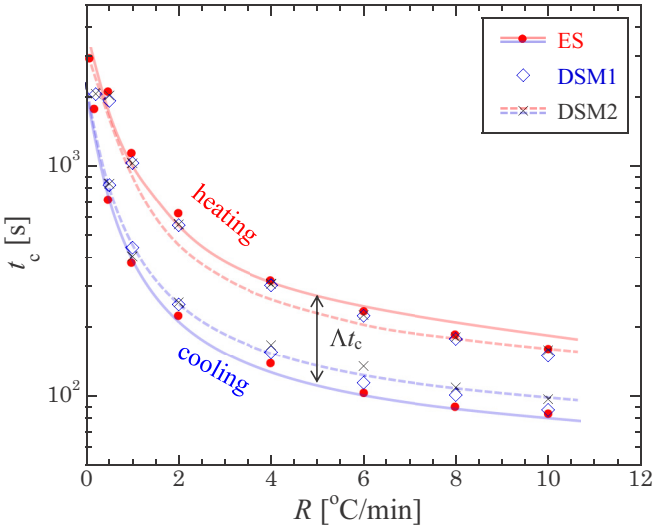

FIG. 8. Critical time $t_c(R)$ in the cooling and heating processes. In comparison with those of ESs ($V = 0$), the curves of NESs (i.e., DSM1 and DSM2) shift to higher t_c in the cooling process, whereas they shift to slightly lower t_c in the heating process. The conditions of DSM1 and DSM2 are the same as those of Fig. 6.

to be varied in ES, DSM1, and DSM2. For example [for heating (+)], $T_{cR0}^{+} = 41.64$, $a = 10.59$, and $\beta = 0.7022$ for ES; $T_{cR0}^{+} = 41.14$, $a = 11.53$, and $\beta = 0.9222$ for DSM2.

Moreover, t_c is given as a function of R in Fig. 8, which depends on V. The difference in critical times, $\Lambda t_c = t_c(\text{CHT}) - t_c(\text{CCT})$, appears to decrease with increasing R (i.e., $R \to \infty$; $\Lambda t_c \to 0$) and this behavior is still maintained in the presence of V. However, $\Lambda t_c = 0$ may not be realized because of the existence of R_c stated in Sec. II A. In Fig. 8, t_c can be expressed as

$$t_c = t_{Rc}^{\pm} + t_{R0}\exp[-\gamma(R/R_c)^{\kappa}]. \tag{5}$$

Here, t_{R0} and $t_{Rc}^{\pm}$ indicate the characteristic values of t_c for $R \to 0$ and $R \to R_c$, respectively, and γ are determined for heating (+) and cooling (−) processes by the least square method; all of them appear to be varied in ES, DSM1, and DSM2. For example [for heating (+)], $t_{R0} = 1.382 \times 10^4$, $t_{R_c}^{+} = 188.2$, $\gamma = 7.162$, and $\kappa = 0.3963$ for ES; $t_{R0} = 8940$, $t_{R_c}^{+} = 176.0$, $\gamma = 7.832$, and $\kappa = 0.5035$ for DSM2.

The shift of the curve of V-originated $T_c(t)$ shows a decrease in T_c from that of ES ($V = 0$), as shown in Figs. 6 and 7; that is, $\Delta T_c = T_c(V) - T_c(0) < 0$. This result shows the possibility of controlling T_c in the presence of applied voltages causing EC. The investigation of $\Delta T_c(V)$ with various values of V (for $V < V_c$ and $V > V_c$) is in progress. Considering their complicated director fields for FT ($V < V_c$), SMT, DSM1, and DSM2 as shown in Fig. 9, $T_c(V)$ should be examined in detail around their bifurcations, and unmentioned ECs such as abnormal [45,46] and bimodal [47,48] instabilities might have to be considered for the investigation of $\Delta T_c(V)$.

It is worth mentioning earlier studies on controlling T_c in NLCs using an electric field not causing EC (i.e., in the case of $V < V_c$) [18,49]. In principle, the free energy density (in cgs units) of the NLC in the presence of the electric field $\boldsymbol{E}$ is

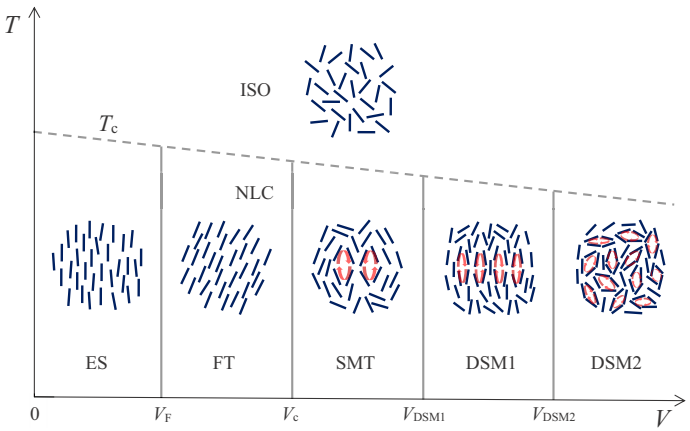

FIG. 9. Schematic diagram for the director fields (in the xz plane) indicating specific phases (ISO and NLC) and ECs (in NLC). Below T_c depending on the director fields, the NLC phase provides ES, Fréedericksz transition (FT), SMT (soft-mode turbulence), DSM1, and DSM2 which strongly depend on V. The line of $T_c(V)$ was not determined in the present study, which may be a more complicated curve by the detail of the director fields and flows including unmentioned instabilities [12,13,45–48].

expressed as [17,18]

$$f_{el} = -\frac{1}{8\pi}[\varepsilon_\perp E^2 + \Delta\varepsilon(\boldsymbol{n}\cdot\boldsymbol{E})^2]. \tag{6}$$

Because the dielectric anisotropy $\Delta\varepsilon = \varepsilon_{||} - \varepsilon_\perp < 0$ for the present MBBA, the second term increases the free energy density f_{el}; accordingly, $\boldsymbol{E}$ destabilizes the NLC state so that the N-I transition can occur more easily than expected for $E = 0$; this may contribute to disordering ($S = 0$) for the N-I transition. Consequently, T_c decreases with an increase in E;

$$\Delta T_c = T_c(E) - T_c(0) \approx \frac{(\varepsilon_{ISO} - \varepsilon_{||})E^2}{8\pi\,\Delta H} \tag{7}$$

where ε_{ISO} is the dielectric constant of the ISO phase (at $T > T_c$), and ΔH is the enthalpy of the N-I transition [18,49]. However, owing to the materials and their shapes, different E dependencies of ΔT_c were found; for example, $\Delta T_c \propto E^2$ for weak E [49], $\Delta T_c \propto E^{2/3}$ for a paraelectric-ferroelectric transition [50], and $\Delta T_c \propto E$ for antiferroelectric-liquid transitions in bent [51,52] or rod shapes [53,54]. To understand the disagreements and limitations of the predictions of Eq. (7) (i.e., $\Delta T_c \propto E^2$) better, other aspects such as the additional free energy density should be considered in Eq. (6) [54]:

$$\Delta f_{el} = \frac{c_1 T}{\sqrt{S}}|E| + \frac{c_2 T}{S}E^2. \tag{8}$$

Here, the first and second terms originate from the director fluctuations with wavelengths longer and shorter than a characteristic coherence length $\xi(E)$ of the fluctuations, respectively; c_1 and c_2 are determined by a typical molecular length. Indeed, this additional contribution is due to the entropy origin, which is not considered in Eq. (6). If the quenching of the director fluctuations by an electric field is dominant, ΔT_c may be changed from Eq. (7). This originates from the decreasing entropy of the state due to quenching which results in an increase in the free energy [54]. Note that these arguments are valid only for ES (i.e., $V \neq 0$, but no EC), in which the principle of free energy minimization holds. However, in the case of NES, where the principle is generally not applicable because it involves EC, various aspects such as secondary instability of EC before DSM2 should be considered. [12,13,45–48]. Moreover, in the case of the I-N transition, similar arguments can be considered but they are also not simple because of the same reasons; note that ΔT_c for the cooling process (i.e., the I-N transition) is more remarkable than that for the heating process (i.e., the N-I transition), as shown in Figs. 6 and 7. In addition, similar to the electric field-dependent T_c, a magnetic field $\boldsymbol{H}$ can also vary T_c through its contribution to free energy density (in cgs units) [17]:

$$f_{mag} = -\tfrac{1}{2}[\chi_\perp H^2 + \Delta\chi(\boldsymbol{n}\cdot\boldsymbol{H})^2]. \tag{9}$$

Because the anisotropy of the magnetic susceptibility $\Delta\chi = \chi_{||} - \chi_\perp > 0$ for the present MBBA, T_c is expected to increase with the strength of H; that is, $\Delta T_c \propto H^2$ [17,55–57]. Similar to the aforementioned $\Delta T_c(E)$, additional aspects should be considered to obtain a more accurate $\Delta T_c(H)$, for example, a biquadratic term (H^4) by considering uniaxial and biaxial NLCs [58]. To compare with $\Delta T_c(V)$, $\Delta T_c(H)$ will be investigated in a future study.

C. Morphological and dynamical features in phase transitions in nonequilibrium systems

Moreover, we observed the optical patterns during the cooling process (at a fixed $R = 4$) in the presence of V. For $V = 28.4$ V causing DSM1, the pattern evolution in the cooling process is displayed in Fig. 10. In comparison with that in ES ($V = 0$) [Fig. 3(b)], a different pattern ($t = 85$) just after $t = t_c = 82$ is found, showing a mosaic pattern including the nucleation of NLC around $T_c(t_c)$; many localized DSM1s grow smoothly ($t = 90$) and combine with one another ($t = 100$), and eventually become a typical DSM1 expanded in the whole cell ($t = 130$, $T = 25$). Furthermore, for much higher voltages ($V \gg V_c$) causing DSM2 ($V = 92.1$ V), the pattern evolution in the cooling process is displayed in Fig. 11. The evolution patterns (Fig. 11) are quite different from those of DSM1 (Fig. 10); no mosaic pattern and no localized DSM2 were found. Apparently, a distinguishable pattern ($t = 93$ and 95) is found before evolving into a typical DSM2 ($t = 130$, $T = 25$), which should be differentiated from a conventional SMT; in particular, the large wave number k_D of the pre-DSM2 ($t = 93$ and 95) completely differs from k_{SMT} of the SMT ($k_D \sim 5k_{SMT}$); this EC pattern will be studied in a future study.

Finally, $I(t)$ was measured for ES ($V = 0$), DSM1 ($V = 28.4$ V), and DSM2 ($V = 92.1$ V) using various cooling rates R (0.5–10), as shown in Fig. 12. For ES, a minimal peak I_{min} indicating the I-N transition is found at t_c [i.e., T_c in Fig. 3(a)], and t_c shifts to a lower value with increasing R; for DSM1, such a shift is also found, but the profile of $I(t)$ fluctuates violently after a maximal peak I_{max} following I_{min} through the appearance of the localized DSM1s (Fig. 10). For DSM2, in contrast, it is found that a universal profile of $I(t)$ with R-independent values of I_{min} and I_{max} is characterized; therefore, the unique $I(t)$ is determined by scaling time (t/t_c),

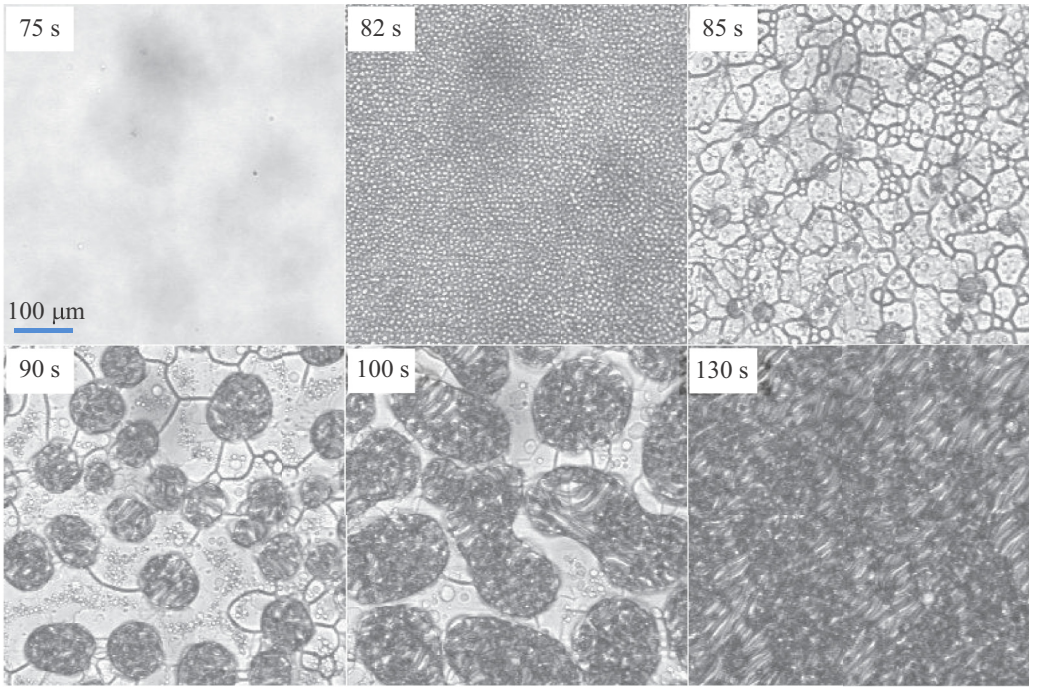

FIG. 10. Pattern evolution of DSM1 in the I-N phase transition ($V = 28.4$ V $> V_c$). Each image was obtained at each time t from the start of a continuous cooling process ($R = 4\,^{\circ}$C/min); $t = 82$ s indicates t_c that is defined in Fig. 3(a), and the pattern at $t = 130$ s shows a typical DSM1. The darker disklike parts at 85 s corresponding to DSM1 of the NLC grow with time ($t = 90$, 100, and 130 s).

as shown in Fig. 13. This universal profile of $I(t)$ for the DSM2 may result from the isotropic property of the DSM2 with fast internal fluctuations, and this feature of the DSM2 was also found in the heating process. This finding is important for predicting the phase transition (i.e., I_{min} for T_c) without considering the cooling rate R. The values of $\Delta I = I_{ISO} - I_{min}$ characterizing the I-N transition for ES, DSM1, and DSM2 can be determined from Fig. 12; in comparison with those

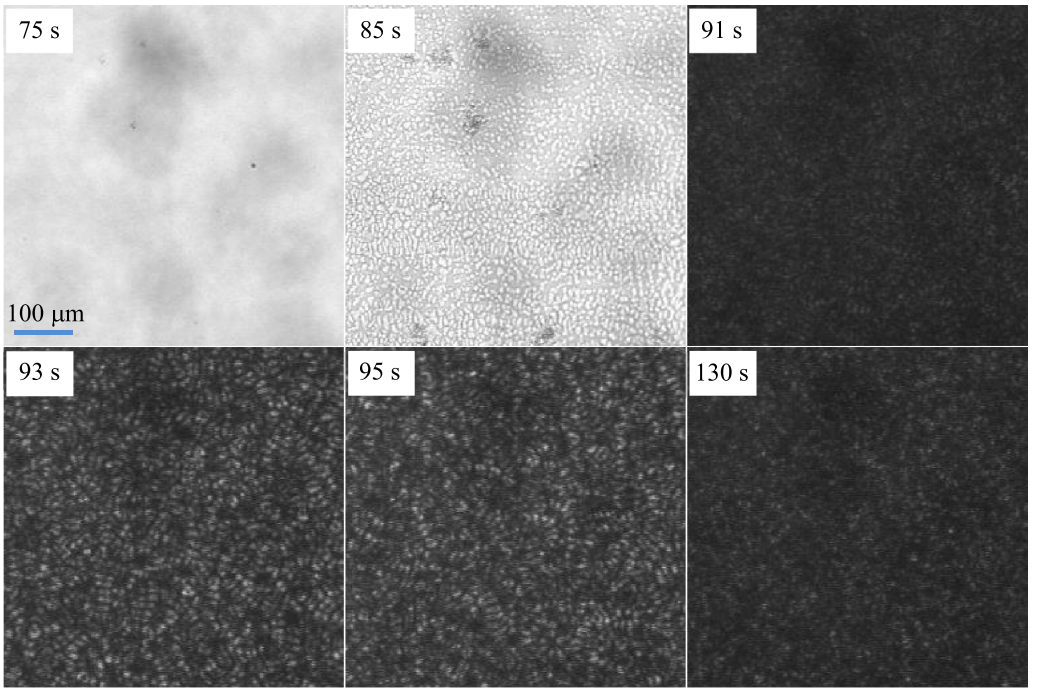

FIG. 11. Pattern evolution of DSM2 in the I-N phase transition ($V = 92.1$ V $\gg V_c$). Each image was obtained at each time t from the start of a continuous cooling process ($R = 4\,^{\circ}$C/min); $t = 91$ s indicates t_c that is defined in Fig. 3(a), and the pattern at $t = 130$ s shows a typical DSM2; compare this evolution to that of DSM1 in Fig. 10, and also that of ES in Fig. 3(b).

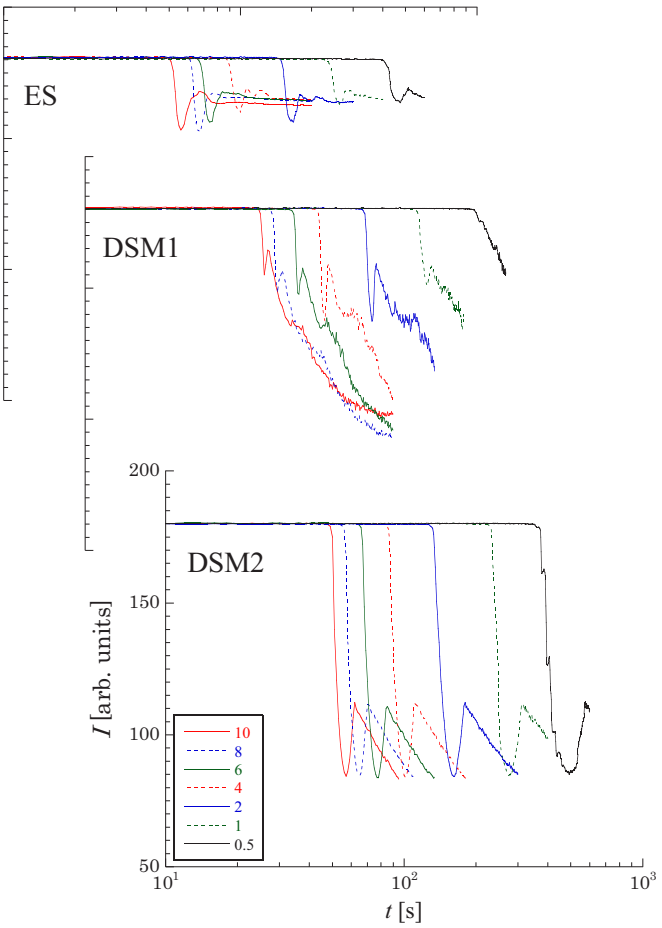

FIG. 12. Averaged optical intensity $I(t)$ with respect to various cooling rates $R(= 0.5–10\,^{\circ}\mathrm{C/min})$. Note $I(t)$ of DSM2 ($V = 92.1$ V), and compare it to those of ES ($V = 0$) and DSM1 ($V = 28.4$ V). The upper two subfigures for the ES and DSM1 have horizontal and vertical axes on the same scale as the main figure.

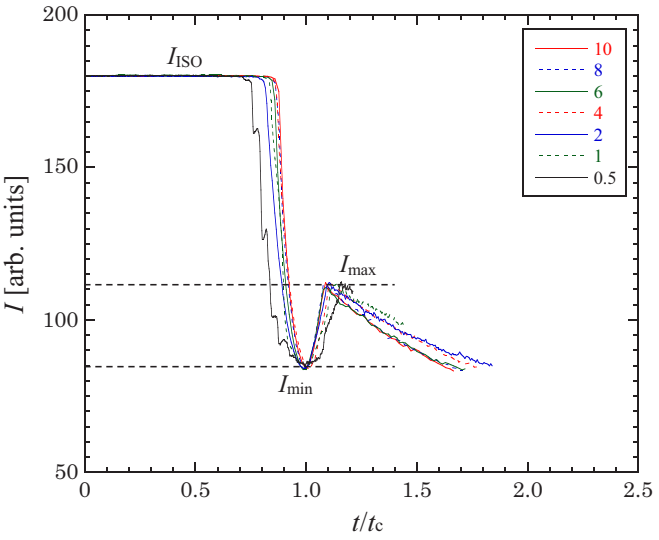

FIG. 13. Scaled $I(t)$as a function of t/t_c with respect to various cooling rates R $(= 0.5–10\,^{\circ}\mathrm{C/min})$ for DSM2 ($V = 92.1$ V). The characteristic intensity I_{min} indicates an R-independent value at $t = t_c$, which gives T_c for the I-N transition [Fig. 3(a)]; moreover, another R-independent peak I_{max} can be determined for DSM2, which differs from those of ES ($V = 0$) and DSM1 ($V = 28.4$ V); see also Fig. 12.

of ES and DSM1, ΔI of DSM2 is independent of R. These results indicate that DSM2 at high voltages may be used to determine T_c (or t_c) and to monitor the phase transitions [i.e., I-N (and N-I)] only by optically measuring $I(t)$ without considering cooling (and heating) rates R. Accordingly, high voltage-driven DSM2 provides us practical applicability for monitoring and controlling critical temperatures in NLCs.

In addition, we examined isothermal TTT diagrams [33,36,37] after cooling or heating treatments (for $t < t_c$) which show similar T_c curves ($V = 0$) found in the CCT and CHT diagrams (Figs. 4–6). In principle, the former can be transformed from the latter [37]. However, in the presence of V ($>V_c$), the TTT diagrams after heating treatments appear to change, showing the collapse of the universal shape of the T_c curve (e.g., Fig. 6). The investigation of the different changes of T_c curves between cooling and heating treatments is in progress.

IV. SUMMARY AND CONCLUSION

In the ES ($V = 0$) and NES [i.e., DSM1 ($V = 28.4$ V) and DSM2 ($V = 92.1$ V)], the phase transitions between the ISO and NLC phases were investigated by continuous cooling and heating processes at various rates $R(= 0.1–10\,^{\circ}\mathrm{C/min})$; in particular, the critical temperature T_c for each transition was determined by a dynamic image-processing method. In ES, the CCT and CHT curves [i.e., $T_c(t)$] give estimated values of $T_{IN} \approx 38.4\,^{\circ}\mathrm{C}$ and $T_{NI} \approx 41.3\,^{\circ}\mathrm{C}$ in the I-N and N-I transitions for MBBA in this study ($t < 10^4$ s), respectively, which are consistent with the nominal value previously reported [42]. Moreover, a critical R_c can be estimated, which indicates a maximal R for measuring T_c; because minimal finite times for ordering ($S \neq 0$) and disordering ($S = 0$) for the I-N and N-I transitions must be needed, the transitions cannot occur for $R > R_c$; $R_c \approx 14.6\,^{\circ}\mathrm{C/min}$ for the I-N transition and $R_c \approx 21.6\,^{\circ}\mathrm{C/min}$ for the N-I transition. No occurrence of the transition for $R > R_c$ is very similar to the conventional supercooling (and superheating) phenomena; future studies need to rigorously investigate such phenomena in the transitions between the ISO and NLC phases in comparison to the normal transitions between the liquid and solid phases (and the liquid and gas phases) [59,60]. In comparison with the CCT and CHT curves of ES, they shift smoothly to lower temperatures with an increase in V. However, the decrease in T_c [i.e., $\Delta T_c = T_c(V) - T_c(0)$] may be more complicated than expected in the theoretical prediction ($\Delta T_c \propto V^2$) [18,49], because various director fields depending on V (Fig. 9) may be induced by secondary instabilities [12,13,45–48]; from this point of view, the investigation of ΔT_c is in progress. In NESs, the optical intensity profile $I(t)$ of dynamic patterns is changed by V; depending on V, unexplainable states such as mosaic patterns ($V > V_c$) and pre-DSM2 ($V \gg V_c$) have been found. In particular, $I(t)$ for high voltages ($V \gg V_c$) causing DSM2 shows an R-independent, universal profile; thus, T_c can be effectively determined, and the phase transitions can be clearly monitored. Therefore, such high voltage-driven turbulence

(DSM2) provides the possibility of controlling the critical temperatures of materials in NESs; furthermore, our results can be applied in material technology in nonequilibrium-based circumstances [23,24].

ACKNOWLEDGMENT

This work was supported by JSPS KAKENHI Grant No. 18K03464.

[1] H. E. Stanley, *Introduction to Phase Transitions and Critical Phenomena* (Oxford University Press, Oxford, 1971).
[2] S. Alexander and J. McTague, Phys. Rev. Lett. **41**, 702 (1978).
[3] J. M. Kosterlitz and D. J. Thouless, J. Phys. C: Solid State Phys. **6**, 1181 (1973).
[4] V. J. Anderson and H. N. W. Lekkerkerker, Nature (London) **416**, 811 (2002).
[5] X. Moya, S. Kar-Narayan, and N. D. Mathur, Nat. Mater. **13**, 439 (2014).
[6] M. H. Bocanegra-Bernal and S. D. De La Torre, J. Mater. Sci. **37**, 4947 (2002).
[7] J. M. Crosthwaite, M. J. Muldoon, J. N. K. Dixon, J. L. Anderson, and J. F. Brennecke, J. Chem. Thermodyn. **37**, 559 (2005).
[8] H. Y. Zhu, Y. Lan, X. P. Gao, S. P. Ringer, Z. F. Zheng, D. Y. Song, and J. C. Zhao, J. Am. Chem. Soc. **127**, 6730 (2005).
[9] R. Graham and T. Tél, Phys. Rev. A **35**, 1328 (1987).
[10] A. Lemarchand and B. Nowakowski, Mol. Simul. **30**, 773 (2004).
[11] E. Dubois-Violette, P.-G. de Gennes, and O. Parodi, J. Phys. **32**, 305 (1971).
[12] S. Kai and W. Zimmermann, Prog. Theor. Phys. Suppl. **99**, 458 (1989).
[13] N. Eber, P. Salamon and A. Buka, Liq. Cryst. Rev. **4**, 101 (2016).
[14] M. C. Cross and P. C. Hohenberg, Rev. Mod. Phys. **65**, 851 (1993).
[15] S. Kai, *Pattern Formation in Complex Dissipative Systems* (World Scientific, London, 1991).
[16] S. Singh, Phys. Rep. **324**, 107 (2000).
[17] P. G. de Gennes and J. Prost, *The Physics of Liquid Crystals*, International Series of Monographs on Physics No. 83, 2nd ed. (Oxford University Press, New York, 1993).
[18] L. M. Blinov and V. G. Chigrinov, *Electrooptical Effects in Liquid Crystal Materials* (Springer, New York, 1994).
[19] G. H. Heilmeier, L. A. Zanoni, and L. A. Barton, Proc. IEEE **56**, 1162 (1968).
[20] J. A. Castellano, *Liquid Gold: The Story of Liquid Crystal Displays and the Creation of an Industry* (World Scientific, Singapore, 2005).
[21] A. Buguin, M.-H. Li, P. Silberzan, B. Ladoux, and P. Keller, J. Am. Chem. Soc. **128**, 1089 (2006).
[22] L. Dong and Y. Zhao, Mater. Chem. Front. **2**, 1932 (2018).
[23] J. M. Zhang, J. Phys. F: Met. Phys. **14**, 769 (1984).
[24] K. Wu, X. Li, H. Wang, W. Guan, X. Wang, Z. Liao, and W. Li, Petrol. Explor. Develop. **39**, 636 (2012).
[25] K. Dan, M. Roy, and A. Datta, J. Chem. Phys. **143**, 094501 (2015).
[26] R. Williams, J. Chem. Phys. **39**, 384 (1963).
[27] E. F. Carr, Mol. Cryst. Liq. Cryst. **7**, 253 (1969); W. Helfrich, J. Chem. Phys. **51**, 4092 (1969).
[28] A. G. Rossberg, A. Hertrich, L. Kramer, and W. Pesch, Phys. Rev. Lett. **76**, 4729 (1996).
[29] Y. Hidaka, J.-H. Huh, K.-I. Hayashi, S. Kai, and M. I. Tribelsky, Phys. Rev. E **56**, R6256 (1997).
[30] J.-H. Huh and S. Kai, J. Phys. Soc. Jpn. **78**, 043601 (2009).
[31] S. Kai and K. Hirakawa, J. Phys. Soc. Jpn. **40**, 301 (1976).
[32] J.-H. Huh, J. Phys. Soc. Jpn. **85**, 024002 (2016).
[33] J. Schroers and W. L. Johnson, Mater. Trans. JIM **41**, 1530 (2000).
[34] G. Szklarz, K. Adrjanowicz, and M. Paluch, Cryst. Growth Des. **18**, 2538 (2018).
[35] H. Martin, P. Amoako-Yirenkyi, A. Pohjonen, N. K. Frempong, J. Komi, and M. Somani, Metall. Mater. Trans., B **52**, 223 (2021).
[36] P. Rocabois, J. N. Pontoire, J. Lehmann, and H. Gaye, J. Non-Cryst. Solids **282**, 98 (2001).
[37] S.-S. Wu, T.-S. Chin, K.-C. Su, and F.-S. Shyr, Jpn. J. Appl. Phys. **35**, 175 (1996).
[38] H. Amm, R. Stannarius, and A. G. Rossberg, Physica D (Amsterdam, Neth.) **126**, 171 (1999).
[39] J.-H. Huh and N. Miyagawa, Phys. Rev. E **103**, 062701 (2021).
[40] A. Pines and J. J. Chang, Phys. Rev. A **10**, 946 (1974).
[41] G. K. L.Wong and Y. R. Shen, Phys. Rev. A **10**, 1277 (1974).
[42] S. Neuenfeld and C. Schick, Thermochim. Acta **446**, 55 (2006).
[43] T. Soltani, J. P. Marcerou and T. Othman, Liq. Cryst. **40**, 165 (2013).
[44] T. Nagaya, T. Takeda, and H. Orihara, J. Phys. Soc. Jpn. **68**, 3848 (1999).
[45] H. Richter, A. Buka, and I. Rehberg, Phys. Rev. E **51**, 5886 (1995).
[46] J. -H. Huh, Y. Hidaka, and S. Kai, Phys. Rev. E **58**, 7355 (1998).
[47] A. Joets, X. D. Yang, and R. Ribotta, Physica D (Amsterdam, Neth.) **23**, 235 (1986).
[48] E. Plaut and R. Ribotta, Phys. Rev. E **56**, R2375 (1997).
[49] W. Helfrich, Phys. Rev. Lett. **24**, 201 (1970).
[50] K. Yoshino, K. Nakao, H. Taniguchi, and M. Ozaki, J. Phys. Soc. Jpn. **56**, 4150 (1987).
[51] W. Weissflog, M. Schröder, S. Diele, and G. Pelzl, Adv. Mater. **15**, 630 (2003).
[52] F. Vita, I. F. Placentino, C. Ferrero, G. Singh, E. T. Samulski, and O. Francescangeli, Soft Matter **9**, 6475 (2013).
[53] T. Yamamoto and I. Nishiyama, Phys. Chem. Chem. Phys. **16**, 26707 (2014).
[54] S. Dhara and N. V. Madhusudana, Europhys. Lett. **67**, 411 (2004); Eur. Phys. J. E **22**, 139 (2007).
[55] P. J. Wojtowicz and P. Sheng, Phys. Lett. A **48**, 235 (1974).
[56] C. Rosenblatt, Phys. Rev. A **24**, 2236 (1981).
[57] J. Shen and C.-W. Woo, Phys. Rev. A **24**, 493 (1981).
[58] N. Ghoshal, K. Mukhopadhyay, and S. K. Roy, Phys. Rev. E **89**, 042505 (2014).
[59] P. G. Debenedetti, J. Phys.: Condens. Matter **15**, R1669 (2003).
[60] Q. S. Mei and K. Lu, Prog. Mater. Sci. **52**, 1175 (2007).